

# Synergy Between Zn Current Collector and K<sup>+</sup> Shielding Additives for High-Performance Na Plating/Stripping

Prakhar Verma, Sanchita Manna, Jayanta Chakraborty, and Sreeraj Puravankara\*

The direct plating/stripping of Na on bare current collectors often results in poor cycling stability and uncontrolled dendrite growth. These two factors significantly hinder the development of high-energy-density and fast-charging energy storage devices. Herein, the synergistic effect between the highly reversible Na plating/stripping on Zn current collectors and a controlled dendrite growth enabled by KPF<sub>6</sub> electrostatic shielding additives is harnessed. A uniform morphology with lower growth/dissolution overpotential is observed for 20 mM KPF<sub>6</sub> additives. The cycle stability enhances from 218 to 376 cycles in the presence of such additives at an areal current density of 0.5 mA cm<sup>-2</sup> and capacity

of 1.0 mAh cm<sup>-2</sup>. Theoretically, a multicomponent phase-field model is developed to bring insights into the Na electrodeposition in the presence of 0, 5, 10, and 20 mM KPF<sub>6</sub> additives. The model successfully correlates the shield formation and predicts its healing effect on Na dendrites. Further, the effectiveness of the electrostatic shield at high overpotential fails due to the large accumulation of Na<sup>+</sup> ions at the interface. The work strives toward the use of metallic Zn current collectors with electrostatic shielding additives to streamline the cell assembly process.

## 1. Introduction

Sodium-ion batteries (SIBs) have garnered worldwide attention because of the high abundance of Na and a similar charge-storing mechanism as lithium-ion batteries (LIBs).<sup>[1–3]</sup> SIBs typically use a hard carbon (HC) anode that suffers from theoretically low specific capacity (300 mAh g<sup>-1</sup>) and a diffusion-limited charge storing mechanism.<sup>[4–6]</sup> Consequently, this results in low energy density (90–160 Wh Kg<sup>-1</sup>) and poor rate capability, making them less suitable for portable applications.<sup>[7,8]</sup> A promising strategy to overcome such challenges involves eliminating the HC anode by direct plating/stripping Na on the current collector.<sup>[9,10]</sup> The theoretically high specific capacity of Na (1166 mAh g<sup>-1</sup>) and a lower redox potential (−2.71 V vs. standard hydrogen electrode) significantly boost the energy density to ≈300 Wh kg<sup>-1</sup> and facilitates fast charging.<sup>[9,11,12]</sup>

However, switching from Na (de)intercalation to plating/stripping mechanism often leads to poor cycling stability and uncontrollable dendrite growth.<sup>[13]</sup> The spontaneous reaction between the electrodeposited Na metal and electrolyte results in the formation of solid electrolyte interface (SEI). The frequent volumetric expansion/compression of SEI during plating/

stripping cycles lead to SEI breakage and reformation, causing sodium loss and poor cycle stability.<sup>[14,15]</sup> In contrast, the preferential deposition of Na metal at the kink sites on the current collector often results in dendrite formation.<sup>[16]</sup> Dendrites possess significant risk of capacity fade and even short-circuit of the cell.<sup>[17]</sup> Therefore, assuring the robustness of SEI and a dendrite-free morphology is indispensable in the development of such anode-free batteries.

Various electrolyte formulations can significantly influence the uniformity and mechanical strength of the SEI.<sup>[18–20]</sup> Ether-based electrolytes are widely reported to form an inorganic-rich SEI that delivers a high Coulombic efficiency (CE) and a fast electrochemical kinetics.<sup>[21]</sup> Recently, Ge et al.<sup>[22]</sup> reported 2-methyltetrahydrofuran (MeTHF)-based dilute electrolyte form an inorganic–organic bilayer SEI that offers high compositional uniformity and mechanical robustness. The theoretical results indicated the higher involvement of anions in the primary solvation sheath and a weaker binding between the Na<sup>+</sup> ions and solvent complex responsible for the superior Na reversibility. Wang et al.<sup>[23]</sup> demonstrated nearly 99.9% CE during Na plating/stripping in NaPF<sub>6</sub> in diethylene glycol dimethyl ether (diglyme) solvent. Liu et al.<sup>[24]</sup> showed stable Na plating/stripping overpotential for over 1000 cycles in 1 M NaPF<sub>6</sub> in diglyme. Therefore, fluoride-rich ether-based electrolytes promotes stable SEI formation and facilitates higher electrochemical reversibility.

The morphology of electrodeposited Na is primarily governed by the nucleation and growth steps.<sup>[25]</sup> A higher nucleation overpotential leads to nonuniform coverage of current collector and dendritic morphology.<sup>[26–28]</sup> Thus, minimizing the nucleation overpotential is an effective strategy toward dendrite-free morphology. Cohn et al.<sup>[29]</sup> demonstrated coating Al current collectors with an ultrathin layer of carbon or HC<sup>[30]</sup> can significantly

P. Verma, S. Manna, S. Puravankara  
School of Energy Science & Engineering  
Indian Institute of Technology Kharagpur  
Kharagpur, West-Bengal 721302, India  
E-mail: sreeraj@iitkgp.ac.in

J. Chakraborty  
Department of Chemical Engineering  
Indian Institute of Technology  
Kharagpur, West-Bengal 721302, India

 Supporting information for this article is available on the WWW under https://doi.org/10.1002/batt.202500396

lower the nucleation overpotential and facilitate uniform Na plating. Hou et al.<sup>[31]</sup> reported coating Cu current collector with PVDF promotes stable SEI rich in NaF and the faster diffusion of Na<sup>+</sup> ions suppressing dendrite growth. Dahunsi et al.<sup>[32]</sup> evaluated Na plating behavior on Al, Cu, and Zn current collectors in 1 M NaPF<sub>6</sub> in diglyme electrolyte. The electrochemical tests showed a higher CE of 99.90% and longer cycle life for Na cycling on Zn current collectors. Cooper et al.<sup>[33]</sup> concluded the higher compatibility between Zn and Na is due to the lowest lattice misfit between the atoms at the row and plane (<10%) sites as compared to other metallic current collectors such as Cu, Al, and brass. A nitrogen-anchored Zn single atom dispersed over carbon substrate was proposed by Yang et al.<sup>[34]</sup> has shown nearly zero nucleation overpotential, leading to uniform sodium nucleation. Composite Zn materials such as ZnIn<sub>2</sub>S<sub>4</sub> in combination with CNT exhibit excellent sodophilicity and remarkable electrochemical properties.<sup>[35]</sup> However, the complexities and economic viability of synthesizing such composites at a large scale is a matter of concern.

Apart from regulating the nucleation overpotential, the dendrite growth can be suppressed by uniformly distributing the cationic flux across the current collector,<sup>[36,37]</sup> designing solid-state electrolytes with enhanced mechanical strength<sup>[38]</sup> and the use of concentrated electrolytes.<sup>[39]</sup> Numerous theoretical studies indicate that the high electric field along the dendrite tips drives the cationic flux toward them, resulting in faster reaction kinetics.<sup>[40–42]</sup> The nonsacrificial self-healing electrostatic shielding (SHES) additives such as CsPF<sub>6</sub>, RbPF<sub>6</sub>, LiPF<sub>6</sub>, and KPF<sub>6</sub> have shown promising results in suppressing the dendrite growth.<sup>[43–46]</sup> Ding et al.<sup>[47]</sup> demonstrated the working principle of SHES additives for Li plating on a Cu substrate by adding a trace amount of CsPF<sub>6</sub> in 1 M LiPF<sub>6</sub> and propylene carbonate (PC) solution. During the alkali metal electrodeposition, a cationic shield forms around the dendritic protuberance that electrically repels the incoming alkali ions and mitigates the localized growth of such tips.<sup>[46,48]</sup> Shielding additives such as ionic liquid<sup>[49]</sup> and KPF<sub>6</sub><sup>[50]</sup> have shown promising results in preventing the dendrite growth in Li metal anodes. Further, hybrid batteries harness protective shield formation by using multi-ion transport and are a promising avenue for dendrite-free hybrid alkali metal batteries.<sup>[51,52]</sup> The use of KPF<sub>6</sub> salt is an economical choice for suppressing dendrites in anode-free sodium metal batteries.<sup>[53,54]</sup>

In this work, we have incorporated the synergistic effect of lower nucleation overpotential of Zn current collector with a trace amount of KPF<sub>6</sub> additives to obtain dendrite-free sodium plating/stripping. We find KPF<sub>6</sub> containing electrolyte improves the initial Na deposition on the Zn current collector with a lower Na degradation. The electrostatic shield formation of K<sup>+</sup> cations imparts lower overpotential and promotes uniform morphology even at higher current density. Further, the phase-field theory is employed to investigate the electrostatic shield formation and obtain the optimum cationic concentration for effective dendrite mitigation. The phase-field model brings mechanistic insights into the working principle of electrostatic shielding additives.

## 2. Results and Discussion

### 2.1. Zinc Anode Initialization for Uniform Sodium Plating/Stripping

The electrodeposition/dissolution of Na on the polished Zn current collector is investigated comparatively for 1 M NaPF<sub>6</sub> in diglyme (NaPF) and 1 M NaPF<sub>6</sub> with 20 mM KPF<sub>6</sub> in diglyme (NaPF-K) electrolytes. Figure 1a and b shows the cyclic voltammetry (CV) measurement for the freshly prepared cell with Na as the counter and reference electrode for both the electrolyte compositions. During the first segment of CV (0 V–1 V), no peak current is observed and verifies the absence of any Na metal on the Zn current collector. This step also removes any surface impurities on the Zn surface and enhances Na plating.<sup>[29]</sup> Between 0 V and –0.15 V, the first reduction of Na metal takes place on the Zn foil. For NaPF electrolytes, a smaller reduction current denotes lower Na plating than NaPF-K electrolytes. During oxidation, a higher current density is observed in NaPF-K electrolyte that denotes higher stripping efficiency. The CV measurements were repeated for five consecutive cycles to observe the reversibility of Na plating/stripping on the Zn current collector. Zn current collector with NaPF-K electrolyte showed highly reversible Na plating/stripping behavior with nearly no loss in oxidation peak current. Also, the successive CV curves overlapped completely for each cycle. Figure 1c displays the cycle-wise comparison between the CE of Na plating/stripping in both electrolytes. During second cycle, a higher loss in CE is observed for the NaPF electrolyte, and even after 5th cycle, the CE for the NaPF electrolyte is lower than NaPF-K. The other purpose of executing CV cycles on bare Zn foil is to form a Na matrix that lowers the subsequent nucleation overpotential and improves electrochemical reversibility.<sup>[55]</sup> The improved and highly stable CE during successive cycles in the presence of NaPF-K electrolyte imparts the formation of a stable sodium matrix on the Zn current collector. Further, to investigate the role of exchange current density, the Tafel plot for both the electrolytes is shown in Figure 1d. A higher exchange current density of 1.05 mA cm<sup>-2</sup> is observed for NaPF-K electrolyte as compared to 0.72 mA cm<sup>-2</sup> for NaPF electrolytes. The higher exchange current density denotes the faster reaction kinetics and facile electrodeposition/dissolution of sodium on the Zn current collector.

### 2.2. Cycling stability of sodium in presence of KPF<sub>6</sub> additives

The long cycle stability tests on NaPF and NaPF-K electrolytes are investigated comparatively at a constant current density of 0.5 mA cm<sup>-2</sup> and an areal capacity of 1 mAh cm<sup>-2</sup>. The initial CV was performed based on the protocol suggested by Tanwar et al.<sup>[55]</sup> to form a Na matrix on top of bare Zn foil. The Na matrix is believed to provide low overpotential sites for further Na plating. Figure 2a shows the variation in voltage with time during continuous plating/stripping cycles. A voltage-controlled stripping cutoff of 1 V is applied to prevent the accumulation of any reversible Na on the Zn current collector. The cycling of

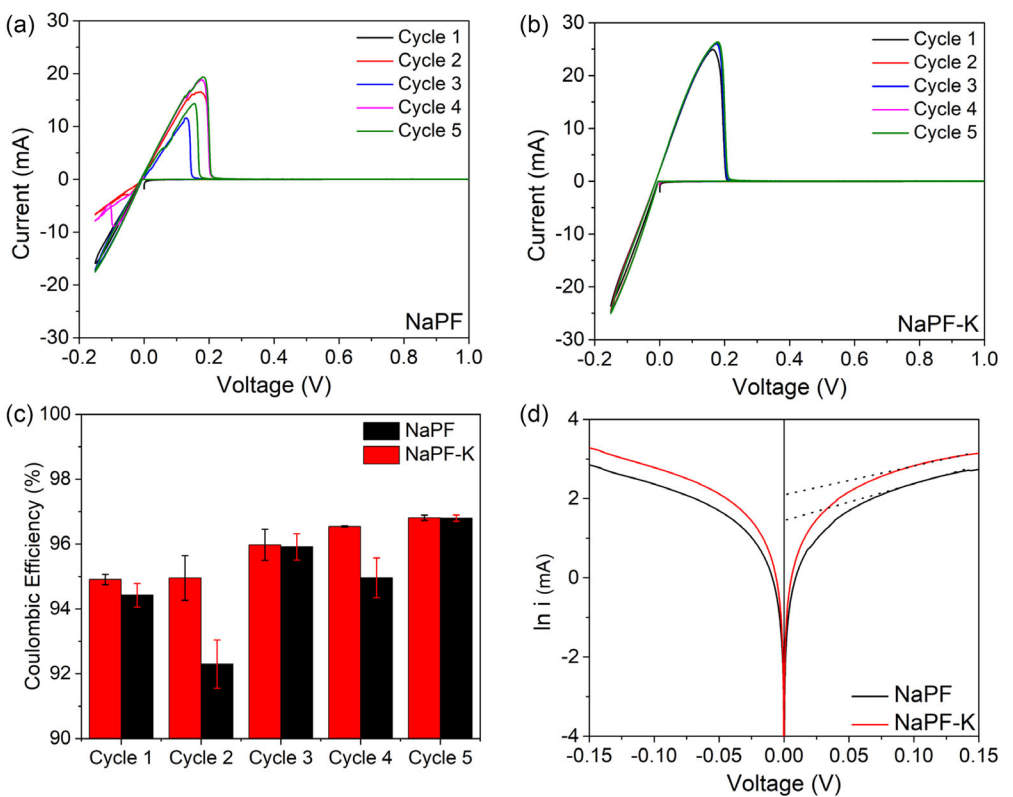


**Figure 1.** Initialization of bare Zn foil by CV for five successive cycles in a) NaPF and b) NaPF-K electrolytes. c) The CE after each CV cycle and d) Tafel plot comparisons for first CV cycle.

NaPF electrolytes shows instability in the overpotential beyond 200 h. The overpotential further increases until 400 h and then stabilizes at  $\approx 9.2$  mV. The cell short-circuits within 900 h of cycling (218 cycles). Contrarily, the NaPF-K electrolyte enhances the cycling stability to more than 1500 h (376 cycles) with no short-circuit. Also, the rise in overpotential in such a cell is observed beyond 700 h of continuous plating/stripping. The early onset of high overpotential in NaPF electrolyte accelerates the dendrite growth and is the primary cause for the early short-circuit.<sup>[56]</sup> However, the presence of KPF<sub>6</sub> additives enhance the cycling stability by lowering the overpotential. The NaPF-K cell do not show dendritic short-circuit even after 500 cycles, although the instability in voltage profile are observed due to the electrolyte decomposition. Both cells show excellent CE because of the higher interfacial stability between Zn and Na metal. Figure 2b shows the CE comparison between the two electrolyte compositions. The CE for NaPF and NaPF-K electrolytes are reported as 99.91% and 99.96%, respectively. Figure S1, Supporting Information, shows the voltage versus capacity plot for average Faradaic efficiency (FE) measurements. The average FE for NaPF and NaPF-K electrolytes are calculated as 99.84% and 99.90%, respectively. The comparative assessment of electrochemical performance of Na plating/stripping on various current collectors reported in the literature are summarized in Table S1, Supporting Information. Clearly, the presence of KPF<sub>6</sub> additives in ether-based electrolytes enhances the cyclic stability and CE of the cell.

Figure 2c comparatively displays the nucleation and growth overpotential at an interval of 100 cycles until cell malfunction. The nucleation overpotential in NaPF electrolyte rises directly from 7.2 to 8.3 mV within the first 100 cycles. Further, the overpotential reaches up to 8.7 mV before getting short-circuited. Similar trends during the stripping cycle are reported as the voltage rises well before reaching the plated capacity of  $1 \text{ mAh cm}^{-2}$  with an increase in cycle number. However, for NaPF-K electrolytes, the rise in overpotential is gradual with cycling, and even after 300 cycles, the nucleation overpotential is well below 8 mV. Figure 2d summarizes the enhanced average CE and extended cycle life (376 cycles) of NaPF-K electrolytes as compared to the NaPF electrolytes (218 cycles).

In addition, Figure 3 shows the ex situ scanning electron microscopy (SEM) characterizations of Zn current collector after 100th and 200th cycle for NaPF and NaPF-K cells at an areal current density of  $0.5 \text{ mA cm}^{-2}$  and capacity of  $1 \text{ mAh cm}^{-2}$ . Figure 3a,b shows the Na morphology after 100th cycle for NaPF and NaPF-K electrolytes, respectively. A nonuniform and highly porous deposition of Na over Zn current collector is observed in NaPF electrolyte (pores highlighted in Figure 3a). Contrarily, NaPF-K electrolytes show a dense electrodeposition with smaller Na particles. The shape of electrodeposited Na particles is spherical and uniformly distribution across the Zn current collector. Figure 3c and d show the SEM morphology after the 200th cycle for NaPF and NaPF-K electrolytes, respectively. The morphology of Na in NaPF electrolyte shows dendrites as

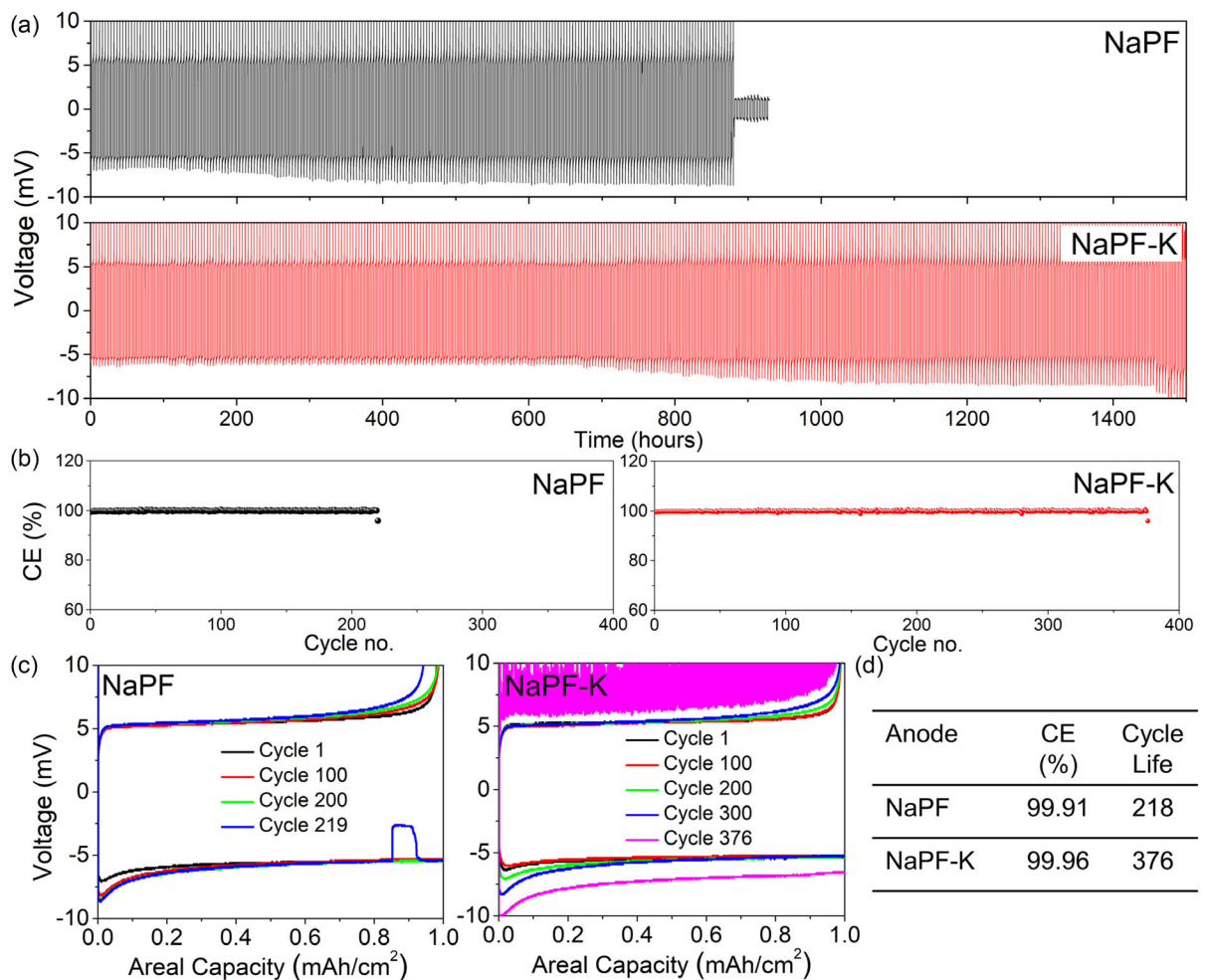


**Figure 2.** Long cycle stability test for a) NaPF and NaPF-K electrolytes, b) CE comparison between the two electrolyte compositions, and the c) overpotential during plating/stripping of Na on Zn current collector at an areal current density of  $0.5 \text{ mA cm}^{-2}$ . d) Summary of the average CE and cycle life using NaPF and NaPF-K electrolytes.

highlighted in Figure 3c. The higher overpotential observed during Na plating/stripping cycles is responsible for the growth at tips leading to such morphological evolution.<sup>[57,58]</sup> Contrarily, NaPF-K electrolytes show a coherent growth of particles with a highly dense Na morphology. The shielding of tip sites by K<sup>+</sup> cations is responsible for arresting the uniaxial growth and homogenizing the Na<sup>+</sup> flux. The energy dispersive X-ray (EDX) analysis was done at the end of life for NaPF and NaPF-K cells to investigate the chemical compositions of SEI at the Zn current collector. Figure S2, Supporting Information shows, the EDX spectrum with the higher K peaks for NaPF-K samples and are responsible for shielding the dendritic protuberance by locally repelling Na<sup>+</sup> flux. Also, as observed in Table S2, Supporting Information, the higher F content in NaPF-K cell is due to higher concentration of PF<sub>6</sub><sup>-</sup> that results in a stable SEI formation and a lower degradation of active Na metal.<sup>[59]</sup> Figure S3, Supporting Information, also reveals morphology of plated Na after 100th cycle at a lower current density of  $0.1 \text{ mA cm}^{-2}$  for the both the electrolytes. NaPF electrolyte show needle-like dendrites whereas NaPF-K electrolyte shows uniform distribution of spherical Na particles. Therefore, clearly

the presence of K<sup>+</sup> cations hinders the initiation of needle morphology and promotes uniform deposition. The sodium plating/stripping performance at a high current rate is further investigated in the next section.

### 2.3. Na Plating/Stripping on Zn Current Collector at High Current Rate

The performance of Na deposition/dissolution on Zn current collector at higher current density was confirmed for a fixed plating capacity of  $1 \text{ mAh cm}^{-2}$ . Figure 4a,b shows the comparison between the overpotential of NaPF and NaPF-K samples as a function of areal capacity. An outstanding electrochemical reversibility of Na is observed for both electrolyte compositions, even at high current density. The average CEs at a current density of  $2.5 \text{ mA cm}^{-2}$  for NaPF and NaPF-K electrolyte is 99.79% and 99.93%, respectively. However, at higher current density, a large overpotential is observed in the NaPF electrolyte. The difference in overpotential between the two electrolyte compositions further rises with an increase in current density. Figure 4c shows

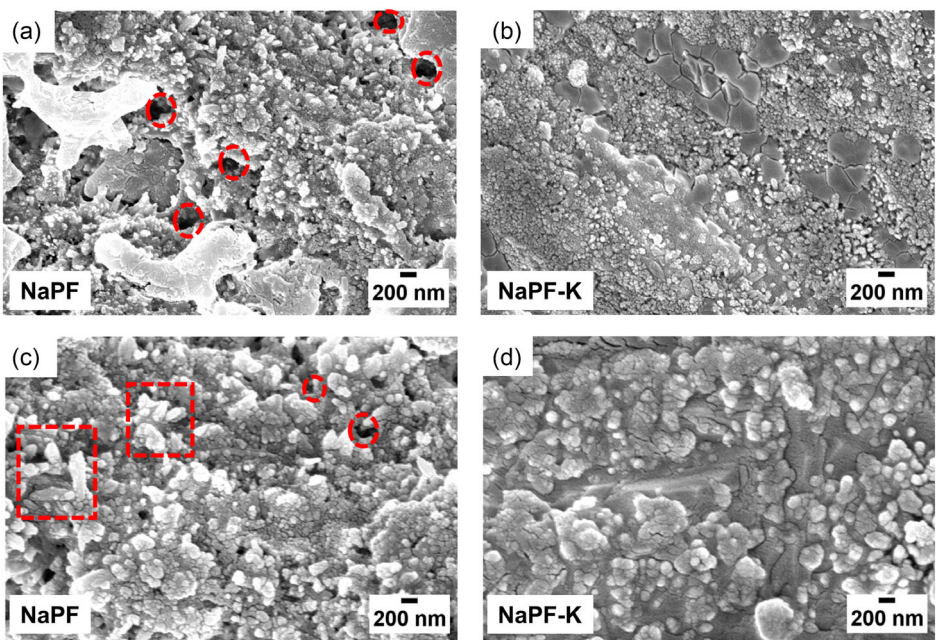


**Figure 3.** Ex situ SEM images of Na morphology on Zn foil at a) 100th cycle with NaPF, b) 100th cycle with NaPF-K, c) 200th cycle with NaPF, and d) 200th cycle with NaPF-K electrolyte at an areal current density of  $0.5 \text{ mA cm}^{-2}$  and capacity of  $1 \text{ mAh cm}^{-2}$ .

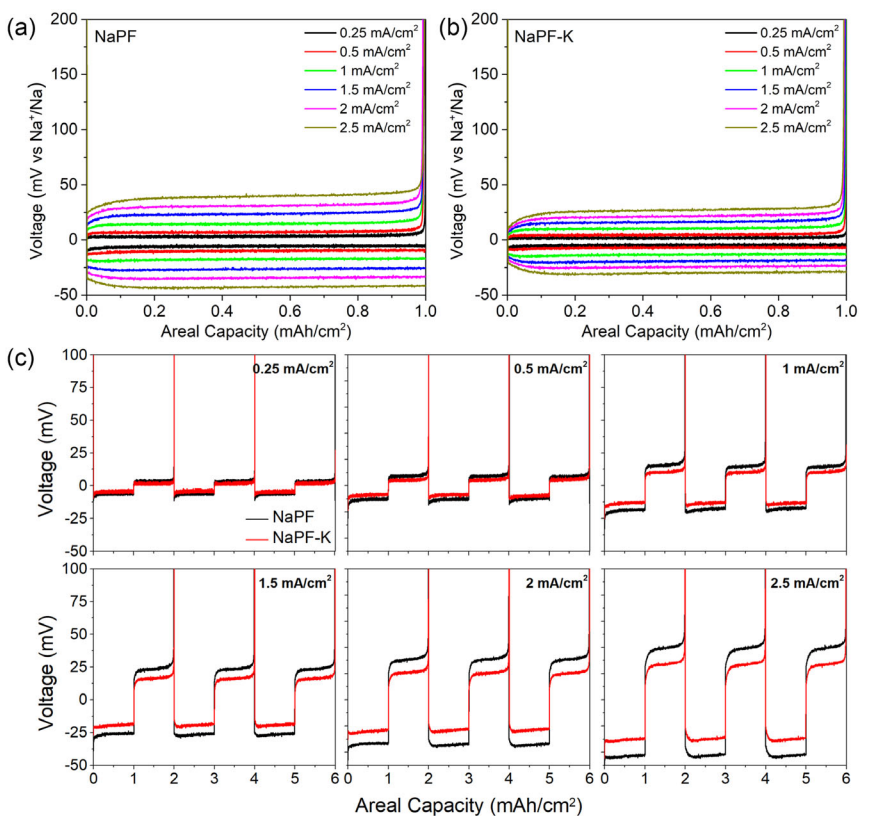


**Figure 4.** Comparison between the rate performance of a)  $\text{KPF}_6$  additive-free electrolyte and b) 20 mM  $\text{KPF}_6$  additive in 1 M  $\text{NaPF}_6$  diglyme electrolyte, and c) cycle wise comparison in the voltage profile during successive plating and stripping.

the difference between cell voltage for the initial three cycles at various current densities. The increase in voltage at higher current density indicates inefficiency during plating/stripping. The higher

overpotential in NaPF cells is due to the poor surface coverage on the Zn current collector, leading to a higher driving force requirement for the growth of Na. Further, the higher overpotential

implies the formation of an unstable interface with higher charge transfer resistance. Such increases in overpotential were previously observed by reference<sup>[56,60]</sup> during plating/stripping cycles and caused electrochemical irreversibility. The growth overpotential in the presence of  $\text{KPF}_6$  additives was lower and led to higher cycle stability. The  $\text{K}^+$  shield distributes the  $\text{Na}^+$  ions homogeneously due to the ionic repulsion, yielding uniform morphology. Figure S4a, Supporting Information, shows the comparison between the nucleation overpotential of Al, Cu, and Zn current collector with Zn have the lowest overpotential of 2.8 mV. Furthermore, Figure S4b, Supporting Information, shows the nucleation overpotential of Zn in both electrolyte compositions are similar at low current density ( $40 \mu\text{A cm}^{-2}$ ). However, a large difference in nucleation overpotential is reported at a higher C rate between NaPF and NaPF-K cells. Figure S5, Supporting Information, shows the plating voltage profile at an even higher current density. The NaPF electrolyte suffers a very high growth overpotential with significantly visible fluctuations in the voltage profile. A dendritic short-circuit was detected in such cases within second cycle at a current density of  $5 \text{ mA cm}^{-2}$ . In contrast, NaPF-K electrolytes show a stable voltage profile with no short circuit during electrodeposition.

The rate performance in Na-Na symmetric cells for NaPF and NaPF-K electrolytes was investigated to decouple the potential contributions from the Zn-Na interface. Figure S6a,b, Supporting Information shows the comparison between the voltage profile for capacity of  $1.0 \text{ mAh cm}^{-2}$ . A time-controlled cut-off was set during the plating and stripping cycles. As expected, NaPF cells

show high plating/stripping potentials with noticeable instability at a current density higher than  $1.5 \text{ mA cm}^{-2}$ . Such instabilities denote unstable SEI formation that leads to parasitic reactions between Na metal and electrolyte. In contrast, we detect a lower plating/stripping overpotential in the presence of NaPF-K electrolytes. A stable voltage profile is achieved for plating/stripping at current densities higher than  $1 \text{ mA cm}^{-2}$ . Further, the mechanistic insights into the  $\text{KPF}_6$  shielding additives on the self-healing of Na dendrites are investigated using phase-field modeling.

#### 2.4. Phase-Field Simulation of Na electrodeposition in presence of $\text{KPF}_6$ additive

Phase-field simulation is a widely used tool to model the morphological evolution of dendrites in Li/Na metal batteries. Figure 5 displays the effect of  $\text{KPF}_6$  additive concentration on the morphology of Na dendrites. The initial Na morphology is identical for all four samples having 0, 5, 10, and 20 mM concentrations of  $\text{KPF}_6$  in 1 M NaPF<sub>6</sub> salt dissolved in diglyme solvent. The ripples in initial morphology were obtained by inserting a Langevin noise of magnitude 0.04. A constant overpotential of  $-0.45 \text{ V}$  is applied in all the aforementioned cases. For additive-free (0 mM) and 5 mM concentrations of  $\text{KPF}_6$ , the tips have insignificant shielding effect, and the growth rate remains unaffected. However, a sluggish growth of tips is observed upon increasing the additive concentration to 10 mM and 20 mM. The broadening of dendrite is observed due to increased reduction of  $\text{Na}^+$  ions laterally than the tip sites.

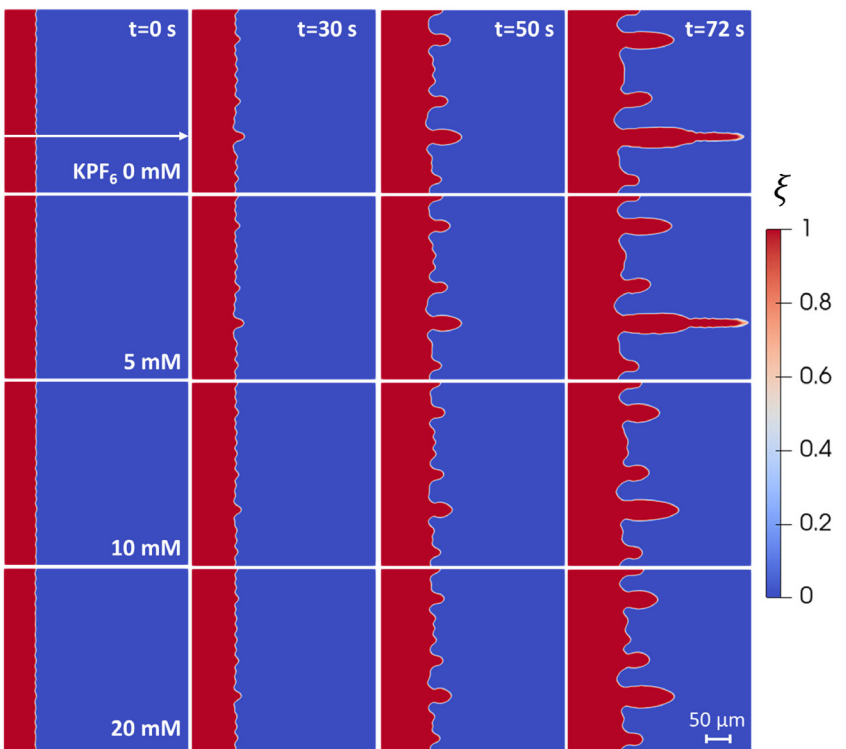


**Figure 5.** Effect of  $\text{KPF}_6$  additive concentration (0, 5, 10, and 20 mM) in 1 M NaPF<sub>6</sub> salt dissolved in diglyme electrolyte on the morphological evolution of Na dendrites at different time selections (0, 30, 50, and 72 s).

Figure S7, Supporting Information, compares the dendrite growth velocity of the most prominent dendrite (line profile highlighted in Figure 5) for various additive concentrations. The initial oscillation in the dendrite tip velocity is due to the dynamic competition between the  $\text{Na}^+$  mass-transfer in electrolyte and the reaction kinetics at the interface.<sup>[40]</sup> At  $t = 18$  s, the tip growth velocity for 10 mM and 20 mM additive concentration deviates from the 0 and 5 mM  $\text{KPF}_6$  samples. The shielding of  $\text{Na}^+$  ions at  $t = 18$  s onward results in the reduction of growth velocity. At  $t = 50$  s, a further suppression in dendrite growth rate is observed for 20 mM samples compared to 10 mM. For  $t > 50$ , the rapid jump in dendrite growth velocity for 0 mM and 5 mM  $\text{KPF}_6$  additive samples depicts the short-circuit. Contrarily, no significant jump in 10 mM and 20 mM  $\text{KPF}_6$  samples implies the effectiveness of cationic shield across the dendrite tips.

Further, results indicate that increasing the concentration of  $\text{KPF}_6$  10 to 20 mM does not significantly improve the dendrite morphology. The experimental observations from NaPF and NaPF-K samples can be directly correlated with 0 and 20 mM  $\text{KPF}_6$  simulated cases, respectively. The extended cycle stability in NaPF-K electrolytes is mainly because of the suppression of the dendritic tips. The highly porous dendrites in NaPF electrolyte are due to the accelerated growth of tips, whereas the ionic repulsion of  $\text{Na}^+$  ions at the tips results in suppressed growth. Furthermore, the broadening of needle morphology in NaPF-K samples relates to the side growth of dendrites due to the ionic repulsion of  $\text{Li}^+$  ions at the tips. The difference between  $\text{Na}^+$  concentration field in NaPF and NaPF-K electrolytes is further investigated to understand the mechanism of shielding effect.

Figure 6 displays the  $\text{Na}^+$  molar concentration in NaPF and NaPF-K electrolytes along the line profile as marked in Figure 5. We observe no accumulation of  $\text{Na}^+$  ions in NaPF electrolyte, as there are no  $\text{K}^+$  ions to prevent the  $\text{Na}^+$  reduction. The peaks observed at  $t = 60$  s and 70 s are due to an extremely high electric field around the dendritic tip, leading to reaction-limited growth. For NaPF-K electrolytes, during early electrodeposition ( $t < 20$  s), no accumulation of  $\text{Na}^+$  ions indicates that the  $\text{K}^+$  concentration field requires some time to form a shield strong enough to repel  $\text{Na}^+$  ions. Later, the higher accumulation of  $\text{K}^+$  ions due to electric migrations leads to the initialization of the protective shield. The repulsion between  $\text{Na}^+$  and  $\text{K}^+$  ions results in the accumulation of  $\text{Na}^+$  ionic species at the interface. Subsequently, for  $t > 30$  s, the  $\text{Na}^+$  molar concentration rises along the cationic shield and triggers the diffusive flux across the interface. Further, to bring crucial insights into the self-healing mechanism of  $\text{KPF}_6$  shielding additives, the effectiveness of the shield and the interactions between  $\text{Na}^+$  and  $\text{K}^+$  ions is investigated.

## 2.5. Mechanistic insights into the self-healing action of $\text{KPF}_6$ additives

Figure 7a shows the Na morphology at  $t = 30$  s with NaPF-K electrolyte. The morphology comprises shorter dendritic protrusions and the most prominent dendrite at  $y = 62 \mu\text{m}$ .

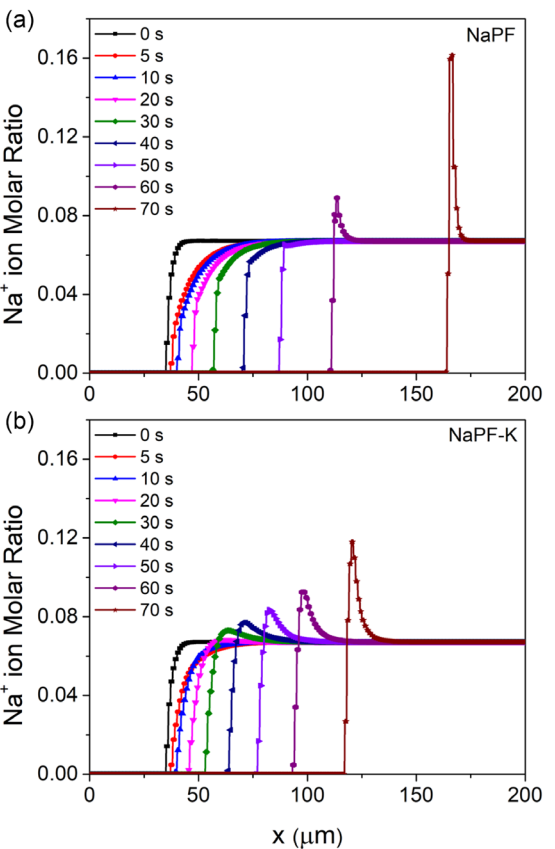
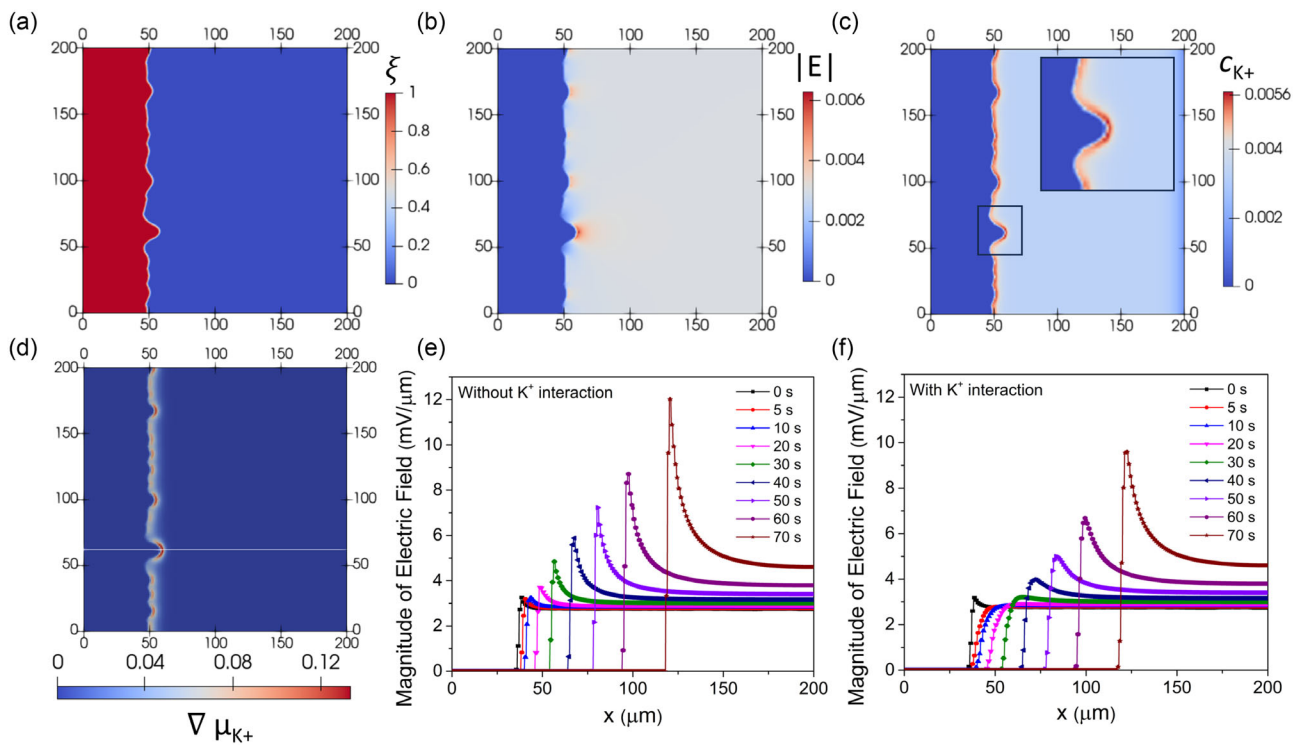


Figure 6. Variation in  $\text{Na}^+$  molar ratio for a) additive-free and b) molar concentration of 20 mM  $\text{KPF}_6$  additive at the line profile of the most prominent dendritic tip.

Such protrusions on the Na surface have a high possibility of growing into dendrites upon further electrodeposition. Figure 7b displays the distribution of electric field magnitude ( $|E|$ ) around the Na metal-electrolyte interface. The higher electric field at the protrusions drives the  $\text{Na}^+$  ions from the bulk of electrolyte toward it. A higher concentration of  $\text{Na}^+$  ions ensures faster growth kinetics of such protrusions. Further, a positive feedback loop involving electric field,  $\text{Na}^+$  concentration, and growth kinetic accelerates the localized electrodeposition.

The self-healing additives work on the principle of forming a shield around the dendritic protrusion. Such cations are not consumed at the interface because of their lower redox potential than  $\text{Na}^+/\text{Na}$ . The shield slows the localized growth by repelling the incoming  $\text{Na}^+$  ions. The coulombic interactions between the  $\text{Na}^+$  and  $\text{K}^+$  ions in the electrolyte phase are studied using multi-component phase-field theory. Figure 7c shows the accumulation of  $\text{K}^+$  ionic species at the higher electric field region and forming a shield-like structure. The relatively higher  $\text{K}^+$  concentration around the protrusion slows the  $\text{Na}^+$  reduction and promotes uniform morphology. Figure 7d shows the gradient of the chemical potential of  $\text{K}^+$  species is higher at the tips and symbolizes higher strength of the  $\text{K}^+$  shield and is expressed using (Equation (3)).

Figure 7e shows the electric field magnitude ( $|E|$ ) without incorporating  $\text{K}^+-\text{Na}^+$  interactions along the line profile marked



**Figure 7.** Cationic shield formation across the Na dendritic protrusions. a) Initial irregular morphology of Na metal ( $\xi$ ), b) electric field magnitude ( $|E|$ ), c) concentration of the accumulated  $K^+$  ions ( $c_{K^+}$ ), and d) the gradient of chemical potential of  $K^+$  ions ( $\nabla\mu_{K^+}$ ) along the Na metal-electrolyte interface. Comparison between the electric field magnitude along the line profile (marked in Figure 6d) for e) NaPF and f) NaPF-K electrolyte at various times during the electrodeposition of Na.

in Figure 7d for 1 M NaPF<sub>6</sub> and 20 mM KPF<sub>6</sub> salts dissolved in diglyme solution. The initial spike in the electric field is due to the small dendritic protrusion in the Na morphology. Gradually, an accelerated growth of such protrusions results in a jump in the electric field distribution. For  $t > 30$  s, an exponential increase in  $|E|$  results in the accelerated growth of the tip. However, once the  $K^+$ -Na<sup>+</sup> interactions in the electrolytes are accounted for, the effective electric field magnitude gets suppressed significantly. Figure 7f shows the electric field magnitude incorporating  $K^+$  interactions. At  $t = 0$  s, the initial electric field is not suppressed because the  $K^+$  cations have not yet accumulated along the dendritic protrusion to form a protective shield. For  $t = 5$  s onward, the cations arrange themselves along the tips, forming a shield-like structure and minimizing the magnitude of the electric field. For  $t \leq 30$  s, the electric field magnitude is completely suppressed in the presence of  $K^+$  cations. However, as Na electrodeposition occurs, the electric field magnitude slowly rises in the presence of  $K^+$  cations. Under such conditions, the delayed electric field accumulates Na<sup>+</sup> ions near the dendrite tips. The higher diffusive flux of Na<sup>+</sup> ions due to a high gradient in the concentration field outplays the repulsive force from  $K^+$  ionic shield and results in the penetration of the shield. This leads to the failure of the electrostatic shield and an accelerated growth of the dendrite tip. Therefore, minimizing the local overpotential at the Na metal and electrolyte interface is necessary for the efficacy of self-healing electrostatic shielding additives.

### 3. Conclusion

In summary, we have demonstrated the synergistic effect of Zn current collector with a trace amount of KPF<sub>6</sub> additive can effectively improve the sodium nucleation and growth morphology. The lower nucleation overpotential for sodium plating on the Zn surface enhances uniform plating. Meanwhile, the electrostatic shielding behavior of the KPF<sub>6</sub> additive improves the dendrite growth morphology. K<sup>+</sup> also enhances the initial current-collector surface coverage and results in stable CE during the sodium matrix formation. The uniform plating in the presence of  $K^+$  ionic shield results in superior cycling performance at current density of 0.5 mA cm<sup>-2</sup> for the areal capacity of 1 mAh cm<sup>-2</sup>. The cycle stability increased from 220 cycles for the additive-free electrolyte to more than 375 cycles in the presence of 20 mM KPF<sub>6</sub> additive. The SEM measurement also confirms higher density and uniform size distribution of particles in presence of NaPF-K electrolytes. Further, at high current density, KPF<sub>6</sub> significantly reduces electrolyte polarization, causing lower growth overpotential. In addition, the phase-field modeling study was conducted to validate the electrostatic shielding mechanism by incorporating the ion-ion interactions in the multispecies transport equation. The optimum concentration of KPF<sub>6</sub> salt is calculated to be in the range of 10–20 mM. Further, increasing the additive concentration resulted in no significant improvement in sodium morphology due to the higher diffusive flux of Na<sup>+</sup> ions caused by their accumulation at the dendritic tips.

Therefore, we demonstrate a synergistic way to exploit the enhanced nucleation and growth by pairing the Zn current collector with KPF<sub>6</sub> shielding additives.

## 4. Experimental Section

Zn foil was first polished using micro grit sandpaper to remove the oxide layer. The polished Zn foil was then cleaned using ethanol and acetone twice before placing it in the vacuum oven at 80 °C for 2h for drying. The dried Zn foil was cut into discs of diameter 16 mm. Whatman glass fiber (GF/C) membrane was cut into 19 mm diameter discs and was used as a separator. All the materials were transferred into the glove box. The baseline electrolyte was prepared by dissolving 1 M NaPF<sub>6</sub> salt in diethylene glycol dimethyl ether (diglyme) solvent, and the electrolyte was named as NaPF. Following, 20 mM KPF<sub>6</sub> salt was dissolved in an equivalent NaPF electrolyte and was denoted as NaPF-K. The sodium metal electrodes were cut from sodium cubes and placed over the separator. The sodium metal loading was near 15 mg cm<sup>-2</sup>. All the electrochemical testings were done using CR 2032 type coin cells, assembled in the argon-filled glove box at O<sub>2</sub> and H<sub>2</sub>O concentrations less than 0.1 ppm. The assembled cells were rested for 12 h before performing electrochemical characterizations.

The CV and rate performance tests were carried out on WaveDrive 100 Potentiostat/Galvanostat. The initial voltage for CV was 0 V and was cycled upside between -0.15 to 1 V at a sweep rate of 0.1 mVs<sup>-1</sup>. The long cycling tests were performed on the Neware battery testing cycler at 0.5 mA cm<sup>-2</sup>. All the long cycled cells were disassembled and dried inside the glove box overnight before taking out for the ex situ SEM measurements (ZEISS, MERLIN). The average FE was quantified using the protocol developed by Adams et al.<sup>[61]</sup> Na metal was first electrodeposited over the bare Zn foil at 0.5 mA cm<sup>-2</sup> for a total areal capacity (Q<sub>T</sub>) of 1.5 mAh cm<sup>-2</sup>. Later, the cell was stripped and plated at an areal current density of 0.5 mA cm<sup>-2</sup> for capacity (Q<sub>c</sub>) of 0.5 mAh cm<sup>-2</sup> for 100 consecutive cycles. On completion of the 100th cycle, the remaining active Na was stripped, and the stripping capacity (Q<sub>s</sub>) was quantified. Finally, the average FE was calculated using (Equation (1)). All the reported measurements were performed at room temperature

$$FE_{avg} = \frac{nQ_c + Q_s}{nQ_c + Q_T} \quad (1)$$

## Phase-Field Modeling

A grand-potential phase-field model to simulate the electrodeposition of sodium with NaPF and NaPF-K electrolyte was developed for a multicomponent system. The simulation system comprise two phases: Na metal (solid) and electrolyte. The solid phase comprises only Na atoms, and the electrolyte phase comprises Na<sup>+</sup>, K<sup>+</sup>, PF<sub>6</sub><sup>-</sup> ions, and neutral species. There was no reduction of K<sup>+</sup> ion in the solid phase because of its relatively lower reduction potential than Na<sup>+</sup>. Table S3, Supporting Information compares the redox potential between Na<sup>+</sup>/Na and K<sup>+</sup>/K at various molar concentrations. A nonconserved phase-field variable  $\xi$  distinguishes between the two phases. For the solid phase,  $\xi$  is defined as 1 and for the electrolyte phase as, 0. A diffuse interface of thickness 1 μm was considered between the two phases. The spatio-temporal evolution of the solid phase due to electrodeposition is derived using the grand-potential functional<sup>[62]</sup> and is given by (Equation (2))

$$\frac{\partial \xi}{\partial t} = -L_\sigma((\omega_s - \omega_l)h'(\xi) + g'(\xi) - \kappa\nabla^2\xi) - L_\eta h'(\xi) \left\{ \exp\left[\frac{(1-\alpha)nF\eta_s}{RT}\right] - \frac{c_{Li^+}}{c_0} \exp\left[\frac{-anF\eta_s}{RT}\right] \right\} \quad (2)$$

Here,  $L_\sigma$  represents the interfacial mobility coefficient, and  $\omega_s$ ,  $\omega_l$  are the grand-potential density for the solid and electrolyte phases, respectively.<sup>[63]</sup>  $g(\eta)$  is a double-well function corresponding to the stable solid and electrolyte phase.  $g(\eta)$  is expressed as  $W\xi^2(1 - \xi)^2$ , where  $W$  is a switching barrier.  $W$  is related to the surface tension ( $\gamma$ ) and interfacial thickness ( $\delta$ ) as  $W = \frac{3\gamma}{\delta}$ .  $\kappa$  is the gradient coefficient given by  $\kappa = 6\gamma\delta$ .  $L_\eta$  represents the electrochemical reaction rate coefficient.  $h(\xi)$  is an interpolation function defined as  $h(\xi) = \xi^3(6\xi^2 - 15\xi + 10)$ .  $\alpha$ ,  $F$ ,  $R$ , and  $T$  are the transfer coefficient, Faraday constant, universal gas constant, and temperature, respectively.  $\eta_s$  is the surface overpotential and is expressed as  $\eta_s = \eta - E^\theta$ , where  $\eta$  is the potential difference between Na metal and electrolyte phase.  $E^\theta$  is the standard equilibrium half-cell potential measured in reference to the Na metal and is taken 0 throughout the simulation. The current model neglects the influence of mechanical stress on dendrite morphology. Although mechanical stress could impact the electrodeposition through stress-assisted cation diffusion in solid phase and contribute to the variations in the electrochemical overpotential,<sup>[64]</sup> its effect in a liquid electrolyte system is minimal. This simplification was well-supported by prior studies that have observed similar alkali metal growth behavior in liquid electrolytes.<sup>[40,65,66]</sup>

The electrostatic interactions between the Na<sup>+</sup> and K<sup>+</sup> ions in the electrolyte phase was included in the model to investigate its effect on Na electrodeposition. The mass transfer flux of Na and K species is given by (Equation (3) and (4)), respectively. The only mobile species of interest are the Na<sup>+</sup> and K<sup>+</sup> ions

$$J_{Na} = -\frac{D_{Na^+}C_{Na^+}}{RT}(\nabla\mu_{Na} + nF\nabla\eta) - L_{Na^+,K^+}\nabla\mu_K \quad (3)$$

$$J_K = -\frac{D_{K^+}C_{K^+}}{RT}(\nabla\mu_K + nF\nabla\eta) - L_{K^+,Na^+}\nabla\mu_{Na} \quad (4)$$

Here,  $D$  is the diffusivity, and  $C$  is the respective Na<sup>+</sup> and K<sup>+</sup> volume concentration.  $\mu_{Na}$  and  $\mu_K$  are the chemical potentials of Na and K species respectively. The Onsager reciprocal coefficients  $L_{Na^+,K^+}$  and  $L_{K^+,Na^+}$  depicts the cross-effect between Na<sup>+</sup> and K<sup>+</sup> fluxes and are equivalent by symmetry. The evolution of the chemical potential of Na species is obtained by solving the modified diffusion (Equation (5)). Here,  $\chi$  is the susceptibility factor and is expressed using (Equation (6))

$$\frac{\partial\mu_{Na}}{\partial t} = \frac{1}{\chi} \left[ \nabla \cdot J_{Na^+} - \frac{\partial h(\xi)}{\partial t} \left( \frac{C_{Na,m}^s}{C_{Na,m}^l} - c_{Na}^l \right) \right] \quad (5)$$

$$\chi = \frac{\partial c_{Na}^l}{\partial \mu_{Na}} (1 - h(\xi)) + \frac{\partial c_{Na}^s}{\partial \mu_{Na}} h(\xi) \frac{C_{Na,m}^s}{C_{Na,m}^l} \quad (6)$$

$C_{Na,m}^{l,s}$  represents the site density of the Na species in the electrolyte ( $l$ ) and solid ( $s$ ) phase. The local molar ratio of Na in the electrolyte and solid phase ( $c_{Na}^{l,s}$ ) is related to the chemical potential as

$$c_{Na}^{l,s} = \frac{\exp(\frac{\mu_{Na} - \epsilon^{l,s}}{RT})}{1 + \exp(\frac{\mu_{Na} - \epsilon^{l,s}}{RT})} \quad (7)$$

where  $\epsilon^{l,s}$  is the difference in the chemical potential of Na species and neutral components in the electrolyte/solid phase at the equilibrium state. The evolution of the chemical potential of K species is given by (Equation (8)). The K<sup>+</sup> ions because of their lower reduction potential than Na<sup>+</sup> do not participate in electrochemical reactions at the anode.

$$\frac{\partial\mu_K}{\partial t} = \nabla \cdot J_{Na^+} \quad (8)$$

The dependency between grand potential density in solid ( $\omega_s$ ) and electrolyte ( $\omega_l$ ) with chemical potential is given by the dilute solution theory as

$$\omega_s = f_{\min}^s - \frac{k_B T}{V_a} \exp\left(\frac{\mu_{\text{Na}} - E_{\text{Na}}^s}{k_B T}\right) \quad (9)$$

$$\omega_l = f_{\min}^l - \frac{k_B T}{V_a} \exp\left(\frac{\mu_{\text{Na}} - E_{\text{Na}}^l}{k_B T}\right) - \frac{k_B T}{V_a} \exp\left(\frac{\mu_K - E_K^l}{k_B T}\right) \quad (10)$$

Here,  $f_{\min}$  is the free energy density of the phase at equilibrium.  $E$  is the difference between the chemical potential of species (Na, K) with neutral component at initial equilibrium.<sup>[67]</sup>  $E$  is constant for all components and has a dimension of energy. The atomic volume ( $V_a$ ) for all chemical species is assumed same.

The spatial distribution of overpotential ( $\eta$ ) across the two phases is determined using the Poisson's equation

$$\nabla \sigma \nabla \eta = n F C_m^s \frac{\partial \zeta}{\partial t} \quad (11)$$

where the effective conductivity ( $\sigma$ ) along the solid and electrolyte phase is given as  $\sigma = \sigma^s h(\zeta) + \sigma^l(1 - h(\zeta))$ .  $C_m^s$  is the site density of Na in the electrode phase.

Equation (2), (5), (8), and (11) are solved together to simulate the electrodeposition of Na in the presence of NaPF and NaPF-K electrolytes. The dimension of simulation box was 200  $\mu\text{m} \times 200 \mu\text{m}$ . The initial irregular morphology of Na metal was obtained by inserting a Langevin noise of magnitude 0.40 and electroplating for 20 s at a constant overpotential of  $-0.45 \text{ V}$  in NaPF electrolyte. The key simulation parameters and numerical implementation of the model are described in the supporting information Table S4.

## Acknowledgements

The authors thank the Central Research Facility and Param Shakti supercomputing facility established under the National Supercomputing Mission (NSM) at IIT Kharagpur. P.V. acknowledges the Prime Minister's Research Fellowship (PMRF) by the Government of India for financial assistance. S.M. acknowledges DST-INSPIRE for the financial assistance for doctoral research work.

## Conflict of Interest

The authors declare no conflict of interest.

## Data Availability Statement

The data that support the findings of this study are available in the supplementary material of this article.

**Keywords:** cationic shielding additives • phase-field model • sodium dendrites • sodium metal batteries • zinc current collector

- [1] R. Schmuck, R. Wagner, G. Höpfl, T. Placke, M. Winter, *Nat. Energy* **2018**, *3*, 267.
- [2] S. F. Schneider, C. Bauer, P. Novák, E. J. Berg, *Sustainable Energy Fuels* **2019**, *3*, 3061.

- [3] W. Zhang, J. Lu, Z. Guo, *Mater. Today* **2021**, *50*, 400.
- [4] B. Wang, J. R. Fitzpatrick, A. Brookfield, A. J. Fielding, E. Reynolds, J. Entwistle, J. Tong, B. F. Spencer, S. Baldock, K. Hunter, C. M. Kavanagh, N. Tapia-Ruiz, *Nat. Commun.* **2024**, *15*, 3013.
- [5] S. Manna, S. Puravankara, *Next Mater.* **2025**, *7*, 100353.
- [6] S. Manna, P. Verma, S. Puravankara, *J. Power Sources* **2025**, *631*, 236234.
- [7] K. M. Abraham, *Acsl Energy Lett.* **2020**, *5*, 3544.
- [8] J. Deng, C. Bae, A. Denlinger, T. Miller, *Joule* **2020**, *4*, 511.
- [9] T. Yang, D. Luo, Y. Liu, A. Yu, Z. Chen, *iScience* **2023**, *26*, 105982.
- [10] Y. Liu, Y. Zhu, Y. Cui, *Nat. Energy* **2019**, *4*, 540.
- [11] H. Wang, C. Wang, E. Matios, W. Li, *Angew. Chem. Int. Ed.* **2018**, *57*, 7734.
- [12] J. Liang, W. Wu, L. Xu, X. Wu, *Carbon* **2021**, *176*, 219.
- [13] Y. Jung, S. Lee, D. Kim, J. Park, S. J. Kang, Y. Kim, J.-S. Park, W.-G. Lee, *ACS Appl. Mater. Interfaces* **2023**, *15*, 43656.
- [14] M. Mandl, J. Becherer, D. Kramer, R. Möning, T. Diemant, R. J. Behm, M. Hahn, O. Böse, M. A. Danzer, *Electrochim. Acta* **2020**, *354*, 136698.
- [15] B. Sayahpour, W. Li, S. Bai, B. Lu, B. Han, Y.-T. Chen, G. Deysher, S. Parab, P. Ridley, G. Raghavendran, L. H. B. Nguyen, M. Zhang, Y. S. Meng, *Energy Environ. Sci.* **2024**, *17*, 1216.
- [16] R. Rodriguez, K. E. Loeffler, S. S. Nathan, J. K. Sheavly, A. Dolocan, A. Heller, C. B. Mullins, *Acsl Energy Lett.* **2017**, *2*, 2051.
- [17] B. Yadav, C. B. Soni, S. Bera, H. Kumar, V. Kumar, *Electrochim. Acta* **2024**, *507*, 145212.
- [18] G. Assat, J.-M. Tarascon, *Nat. Energy* **2018**, *3*, 373.
- [19] C. Bao, B. Wang, P. Liu, H. Wu, Y. Zhou, D. Wang, H. Liu, S. Dou, *Adv. Funct. Mater.* **2020**, *30*, 2004891.
- [20] Q. Yu, Y. Xiao, S. Zhao, Y. Miao, S. Wan, L. Zhou, J. Rong, G. Hou, S. Chen, *Adv. Funct. Mater.* **2024**, *34*, 2401868.
- [21] S. Wang, S. Weng, X. Li, Y. Liu, X. Huang, Y. Jie, Y. Pan, H. Zhou, S. Jiao, Q. Li, X. Wang, T. Cheng, R. Cao, D. Xu, *Angew. Chem. Int. Ed.* **2023**, *62*, e202313447.
- [22] B. Ge, J. Deng, Z. Wang, Q. Liang, L. Hu, X. Ren, R. Li, Y. Lin, Y. Li, Q. Wang, B. Han, Y. Deng, X. Fan, B. Li, G. Chen, X. Yu, *Adv. Mater.* **2024**, *36*, 2408161.
- [23] C. Wang, Y. Zheng, Z.-N. Chen, R. Zhang, W. He, K. Li, S. Yan, J. Cui, X. Fang, J. Yan, G. Xu, D. Peng, B. Ren, N. Zheng, *Adv. Energy Mater.* **2023**, *13*, 2204125.
- [24] S. Liu, S. Tang, X. Zhang, A. Wang, Q.-H. Yang, J. Luo, *Nano Lett.* **2017**, *17*, 5862.
- [25] P. Verma, S. Puravankara, J. Chakraborty, *J. Phys. Chem. C* **2024**, *128*, 17328.
- [26] A. Pei, G. Zheng, F. Shi, Y. Li, Y. Cui, *Nano Lett.* **2017**, *17*, 1132.
- [27] K. S. Nagy, S. Kazemiabnavi, K. Thornton, D. J. Siegel, *ACS Appl. Mater. Interfaces* **2019**, *11*, 7954.
- [28] V. Pande, V. Viswanathan, *Acsl Energy Lett.* **2019**, *4*, 2952.
- [29] A. P. Cohn, N. Muralidharan, R. Carter, K. Share, C. L. Pint, *Nano Lett.* **2017**, *17*, 1296.
- [30] A. P. Cohn, T. Metke, J. Donohue, N. Muralidharan, K. Share, C. L. Pint, *J. Mater. Chem. A* **2018**, *6*, 23875.
- [31] Z. Hou, W. Wang, Y. Yu, X. Zhao, Q. Chen, L. Zhao, Q. Di, H. Ju, Z. Quan, *Energy Storage Mater.* **2020**, *24*, 588.
- [32] O. J. Dahunsi, S. Gao, J. Kaelin, B. Li, I. B. A. Razak, B. An, Y. Cheng, *Nanoscale* **2023**, *15*, 3255.
- [33] E. R. Cooper, M. Li, Q. Xia, I. Gentle, R. Knibbe, *Acsl Appl. Energy Mater.* **2023**, *6*, 11550.
- [34] T. Yang, T. Qian, Y. Sun, J. Zhong, F. Rosei, C. Yan, *Nano Lett.* **2019**, *19*, 7827.
- [35] Y. Yao, Y. Yang, Z. Wang, M. Guo, P. Liu, Z. Xing, *J. Power Sources* **2024**, *613*, 234917.
- [36] C.-Z. Zhao, P.-Y. Chen, R. Zhang, X. Chen, B.-Q. Li, X.-Q. Zhang, X.-B. Cheng, Q. Zhang, *Sci. Adv.* **2018**, *4*, eaat3446.
- [37] Y. Ren, Y. Zhou, Y. Cao, *J. Phys. Chem. C* **2020**, *124*, 12195.
- [38] Q. Liu, L. Zhang, H. Sun, L. Geng, Y. Li, Y. Tang, P. Jia, Z. Wang, Q. Dai, T. Shen, Y. Tang, T. Zhu, J. Huang, *Acsl Energy Lett.* **2020**, *5*, 2546.
- [39] Z. Lu, H. Yang, Q.-H. Yang, P. He, H. Zhou, *Angew. Chem. Int. Ed.* **2022**, *61*, e202200410.
- [40] Z. Hong, V. Viswanathan, *Acsl Energy Lett.* **2018**, *3*, 1737.
- [41] J. Jeon, G. H. Yoon, T. Vegge, J. H. Chang, *Acsl Appl. Mater. Interfaces* **2022**, *14*, 15275.
- [42] Y. Xiong, B. Yan, Q. Li, C. Zhi, J. Fan, *J. Power Sources* **2024**, *597*, 234162.
- [43] F. Ding, W. Xu, X. Chen, J. Zhang, Y. Shao, M. H. Engelhard, Y. Zhang, T. A. Blake, G. L. Graff, X. Liu, J.-G. Zhang, *J. Phys. Chem. C* **2014**, *118*, 4043.
- [44] B. Yoon, S. Kim, Y. M. Lee, M.-H. Ryoo, *Acsl Omega* **2019**, *4*, 11724.
- [45] H. Dai, K. Xi, X. Liu, C. Lai, S. Zhang, *J. Am. Chem. Soc.* **2018**, *140*, 17515.

- [46] W. Ji, H. Huang, D. Zheng, X. Zhang, T. Ding, T. H. Lambert, D. Qu, *Energy Storage Mater.* **2020**, *32*, 185.
- [47] F. Ding, W. Xu, G. L. Graff, J. Zhang, M. L. Sushko, X. Chen, Y. Shao, M. H. Engelhard, Z. Nie, J. Xiao, X. Liu, P. V. Sushko, J. Liu, J.-G. Zhang, *J. Am. Chem. Soc.* **2013**, *135*, 4450.
- [48] Q. Shi, Y. Zhong, M. Wu, H. Wang, H. Wang, *Angew. Chem. Int. Ed.* **2018**, *57*, 9069.
- [49] J. Zhong, Z. Wang, S. Wang, X. Li, H. Guo, J. Wang, G. Yan, *Appl. Surf. Sci.* **2023**, *622*, 156968.
- [50] J. W. Han, B. K. Park, Y. M. Kim, Y. Sim, V.-C. Ho, J. Mun, K. J. Kim, *Mater. Chem. Front.* **2023**, *7*, 4553.
- [51] Q. Zhang, Y. Lu, L. Miao, Q. Zhao, K. Xia, J. Liang, S.-L. Chou, J. Chen, *Angew. Chem. Int. Ed.* **2018**, *57*, 14796.
- [52] D. Zhou, X. Tang, X. Zhang, F. Zhang, J. Wu, F. Kang, B. Li, G. Wang, *Nano Lett.* **2021**, *21*, 3548.
- [53] J. Li, S. Liu, Y. Cui, S. Zhang, X. Wu, J. Xiang, M. Li, X. Wang, X. Xia, C. Gu, J. Tu, *ACS Appl. Mater. Interfaces* **2020**, *12*, 56017.
- [54] C. Zheng, D. Ji, Q. Yao, Z. Bai, Y. Zhu, C. Nie, D. Liu, N. Wang, J. Yang, S. Dou, *Angew. Chem. Int. Ed.* **2023**, *62*, e202214258.
- [55] M. Tanwar, H. K. Bezabih, S. Basu, W.-N. Su, B.-J. Hwang, *ACS Appl. Mater. Interfaces* **2019**, *11*, 39746.
- [56] J. Pokharel, A. Cresce, B. Pant, M. Y. Yang, A. Gurung, W. He, A. Baniya, B. S. Lamsal, Z. Yang, S. Gent, X. Xian, Y. Cao, W. A. Goddard, K. Xu, Y. Zhou, *Nat. Commun.* **2024**, *15*, 3085.
- [57] T. Liu, Q. Hu, X. Li, L. Tan, G. Yan, Z. Wang, H. Guo, Y. Liu, Y. Wu, J. Wang, *J. Mater. Chem. A* **2019**, *7*, 20911.
- [58] P. Verma, S. Puravankara, M. N. Nandanwar, J. Chakraborty, *J. Electrochem. Soc.* **2023**, *170*, 030529.
- [59] M. Xu, Y. Li, M. Ihsan-Ul-Haq, N. Mubarak, Z. Liu, J. Wu, Z. Luo, J. K. Kim, *Energy Storage Mater.* **2022**, *44*, 477.
- [60] Z. W. Seh, J. Sun, Y. Sun, Y. Cui, *ACS Cent. Sci.* **2015**, *1*, 449.
- [61] B. D. Adams, J. Zheng, X. Ren, W. Xu, J.-G. Zhang, *Adv. Energy Mater.* **2018**, *8*, 1702097.
- [62] L. Chen, H. W. Zhang, L. Y. Liang, Z. Liu, Y. Qi, P. Lu, J. Chen, L.-Q. Chen, *J. Power Sources* **2015**, *300*, 376.
- [63] N. Moelans, *Acta Mater.* **2011**, *59*, 1077.
- [64] T. Zhang, M. Sotoudeh, A. Groß, R. M. McMeeking, M. Kamleh, *J. Power Sources* **2023**, *565*, 232902.
- [65] G. Qi, X. Liu, R. Dou, Z. Wen, W. Zhou, L. Liu, *J. Energy Storage* **2024**, *101*, 113899.
- [66] C.-J. Ko, C.-N. Tai, C.-H. Chen, K.-C. Chen, *J. Energy Storage* **2024**, *97*, 112615.
- [67] L. K. Aagesen, Y. Gao, D. Schwen, K. Ahmed, *Phys. Rev. E* **2018**, *98*, 023309.

Manuscript received: May 23, 2025

Revised manuscript received: July 22, 2025

Version of record online: